RSC Advances

ROYAL SOCIETY OF CHEMISTRY

www.rsc.org/advances

Introduction

Organic solar cells (OSCs) based on bulk heterojunction (BHJ) active layer have been the current research of both academia and industry throughout the worldwide due to their potential use for cost effective and flexible solar energy conversion devices.[1-8] A BHJ active layer consists of a blend of p-type organic semiconductor (donor) and n-type organic semiconductor (acceptor) and sandwiched between two electrodes.[9,10] A record power conversion efficiency of over 10 % have been reported using soluble π-conjugated low bandgap copolymers as donor in single junction BHJ solar cells with device architecture modification.[11-15] Although the copolymer based solar cells has shown excellent photovoltaic performance, the high degree of polymer structures affects the reproducibility of synthesis, purification and the optical and electrochemical properties of final materials. On the other hand, a recent development of small molecules has emerged as an alternative to copolymers owing to their well-defined chemical structure, reproducibility of synthesis, ease of purification and fine tuning of their optical and electrochemical properties.[16-23] Recently, solution processed bulk heterojunction solar cells based on small molecules as donors have shown PCE in the range of 7-10 %,[24-28] which is similar to recently reported polymer solar cells. These high performances are the result of an inter-disciplinary research effort in device optimization, control of interfacial morphology using additives, solvent annealing techniques and the synthesis of new donor small molecules.[21, 29]

In general, the donor material used for BHJ active layer in organic solar cell should exhibits a strong photon absorption in the visible and near infrared region of solar spectrum, suitable molecular orbitals i.e. highest occupied molecular orbital (HOMO) and lowest unoccupied molecular orbital (LUMO) energy levels, high carrier mobility, excellent film nanoscale morphology and good miscibility with fullerene derivatives.[30] In order to achieve above requirements, one approach is design low bandgap small molecules with donor-acceptor (D-A) structure. Among them, acceptor –donor- acceptor (A-D-A) oligothiophenes were used as donor materials for solution processed organic solar cells.[31] It was reported that proper functionalization and substitution in these molecules allow for good processability and control of the molecular orbital energy levels, which not only leads to broad absorption of solar spectrum but also results a high open circuit voltage due to the deeper HOMO energy level and excellent stability toward oxidation.[32] Recently, Mishra et al has introduced fused thiophene (S) –pyrrole (N) based S,N heteroacenes and their acceptor end-capped dicyanovinylene (DCV) derivatives as A-D-A type donor materials[33] and implemented them as donor for vacuum processed BHJSCs and C_{60} as acceptor and achieved promising PCE up

to 6.5 %.[34] Recently same group has achieved a PCE of 4.9% for solution processed BHJ organic solar cells using similar type of A-D-A small molecules as donor, together with $PC_{61}BM$ as acceptor.[32] It was already reported that rigid multi-fused heteroacene structure has been used as donor block in D-A copolymers for efficient BHJ polymer solar cells.[35-41] Bazan and co-workers implemented a penta-fused silaindacenodithiophene unit in a structurally defined D–A–D–A–D molecule and excellent PCEs up to 6.4% have been reached in corresponding solution-processed BHJSCs.[42] Moreover, recently Steck et al have employed acceptor–donor–acceptor (A–D–A) type low band gap hole transport materials (HTM) comprising S,N-heteropentacene central units for solid-state perovskite-based solar cells.[43]

As S,N-heteroacenes have the favorable properties of oligothiophenes, such as good donor ability and high charge carrier mobility and the adaptation of alkoxy substituent adjusts the HOMO level, we have designed and synthesized two low bandgap small molecules with acceptor–donor-acceptor (A-D-A) structure $SN(BTTh_2)_2$ (**J**) and $SN(BTAOTh_2)_2$ (**K**) containing an electron rich planar S,N heteropentacene as central core, flanked with alkoxy substituted and un-substituted benzothiadiazole (BT) and investigated their optical and electrochemical properties, in order to used them as donor along with $PC_{71}BM$ as acceptor for solution processed organic BHJ solar cells. The devices based on cast **J**:$PC_{71}BM$ and **K**:$PC_{71}BM$ active layer showed power conversion efficiency (PCE) of 1.96 % and 1.57%, respectively, and improved up to 6.02% and 5.06% when the active layers are subjected to two steps annealing TSA, i.e. combined thermal annealing followed by solvent vapor annealing. We have employed the separate thermal annealing and solvent vapor annealing, but the PCE was not significantly enhanced.

Experimental part

Materials and instruments

All reagents were purchased from Sigma-Aldrich, TCI and Alfa Aesar. 1H and13C NMR spectra were recorded on a Varian Mercury 300 spectrometer. Elemental analyses were performed with a Carlo Elba Instruments CHNS-OEA 1108 analyzer. Mass spectra were recorded on a JEOL JMS-SX102A instrument. The absorption and photoluminescence spectra were recorded on a Perkin-Elmer Lambda 2S UV-visible spectrometer and a Perkin LS fluorescence spectrometer, respectively. Cyclic voltammetry was carried out with a BAS 100B (Bioanalytical Systems, Inc.). A three electrode system was used and consisted of a non-aqueous reference electrode (0.1 M Ag/Ag^+ acetonitrile solution; MF-2062, Bioanalytical System, Inc.), a platinum working electrode (MF-2013, Bioanalytical System, Inc.), and a platinum wire (diam. 1.0 mm, 99.9% trace metals basis, Sigma-Aldrich) as the

counter electrode. The redox potential of dyes was measured in CH2Cl2with 0.1 M (n-C_4H_9)4NPF6at a scan rate of 50 mV s^{-1} (vs.Fc/Fc+as an external reference).

Synthesis of materials

4,5-(Di-2-ethylhexyl)-2,7-bis(trimethylstannyl)-dithieno[2,3-d:2′,3′-d′]thieno[3,2-b:4,5b′]dip yrrole(**1**) [8], (5'-hexyl-2,2'-bithiophen-5-yl)trimethylstannane (2),[44] and 4-bromo-7-(5'-hexyl-2,2'-bithiophen-5-yl)benzo[c][1,2,5]thiadiazole (4),[45] were synthesized as reported in literture.

(5'-Hexyl-2,2'-bithiophen-5-yl)benzo[c][1,2,5]thiadiazole-(4,5-(Di-2-ethylhexyl) dithieno) [2,3-d:2′,3′-d′] thieno[3,2-b:4,5-b′]dipyrrole (J).

In a N_2 filled glove box a 20 mL glass tube was charged with 4,5-(di-2-ethylhexyl)-2,7-bis (trimethylstannyl)-dithieno [2,3-d:2′,3′-d′]thieno[3,2-b:4,5-b′] dipyrrole (1) (0.51 g, 0.6 mmol),4-bromo-7-(5'-hexyl-2,2'-bithiophen-5-yl)benzo[c][1,2,5]thiadiazole (4) (0.86 g, 1.8 mmol) and $Pd(PPh_3)_4$ (36 mg, 0.03 mmol) and DMF (15 mL), and sealed with a Teflon® cap.[46] The reaction mixture was heated to 200 °C for 3 hours using a Biotage microwave reactor. The reaction mixture was cooled down to the room temperature, then poured into water and extracted with CH_2Cl_2. The solvent was removed by rotary evaporation and the crude product was purified by flash column chromatography on silica gel using a mixture of chloroform and hexane (2 : 1) as eluent. Finally, evaporation of the solvent afforded the targeted compound (**J**), as a dark green powder. Yield 45 %: ^{1}H NMR (300 MHz, CD_2Cl_2): δ 8.46 (s, 2H), 7.83 (d, 2H, J = 3.6 Hz), 7.66 (s, 4H), 7.00 (dd, 4H, J = 4.2 Hz), 6.69 (d, 2H, J = 3.6 Hz), 4.35 (dd, 4H, J = 6.0 Hz), 2.84 (dd, 4H, J = 6.0 Hz), 2.14 (m, 2H), 1.73 (m, 4H), 1.31-1.42 (m, 28H), 0.89-1.01 (m, 18H). ^{13}C NMR (75 MHz, $CDCl_3$): δ 153.05, 152.69, 146.55, 145.74, 139.77, 137.44, 135.58, 131.68, 128.34, 127.05, 126.48, 125.75, 124.56, 124.33, 123.89, 123.56, 122.60, 119.23, 118.38, 114.776, 40.869, 32.31, 32.02, 30.78, 29.70, 29.04, 24.30, 23.62, 23.40, 15.40, 14.55, 13.78, 12.18, 11.09. MS: *m/z* 1262.35 [M^+]. Anal. Calcd. for $C_{68}H_{74}N_6S_9$: C, 64.62; H, 5.90. Found : C, 64. 19 ; H, 5.68.

4-Bromo-7-(5'-hexyl-2,2'-bithiophen-5-yl)-5,6-bis(hexyloxy)benzo[c][1,2,5]thiadiazole (3).

4,7-Dibromo-5,6-bis(hexyloxy)benzo[c][1,2,5] thiadiazole (3) was synthesized as reported in the literature.[47] (5′-Hexyl-2,2′-bithiophen-5-yl) trimethylstannane (**2**) (1.8 g, 4.3 mmol), 4,7-dibromo-5,6-bis(hexyloxy)benzo[c][1,2,5]thiazole (2.26 g, 4.5 mmol) and toluene (50 mL) were added into a 100 mL double-necked round-bottomed flask. The reaction container was de-aerated with argon for 5 min followed by the addition of $Pd(PPh_3)_4$ (0.25 mg, 0.21 mmol)

and de-aeration for another 20 min with argon to remove O_2. After being heated to reflux overnight at 110° C, the reaction mixture was cooled down to the room temperature, then poured into water and extracted with CH_2Cl_2. The solvent was removed by rotary evaporation and the crude product was purified by flash column chromatography on silica gel using a mixture of chloroform and hexane (1 : 3) as eluant. Finally, the compound (**3**) was collected as an orange solid. Yield : 65% ^{1}H NMR (300 MHz, $CDCl_3$): δ 8.43 (d, 1H, J = 4.5 Hz), 7.20 (d, 1H, J = 3.3 Hz), 7.09 (d, 1H, J = 3.6 Hz), 6.72 (d, 1H, J = 4.5 Hz), 4.19 (dd, 2H, J = 6.9 Hz), 4.12 (dd, 2H, J = 6.3 Hz), 2.81 (dd, 2H, J = 7.2 Hz), 1.95-1.87 (m, 4H), 1.65-1.73 (m, 2H), 1.34-1.56 (m, 24H), 0.90-0.96 (m, 9H). ^{13}C NMR (75 MHz, $CDCl_3$): δ 154.79, 151.75, 151.41, 149.84, 146.16, 145.00, 140.05, 134.85, 132.18, 131.91, 131.86, 125.26, 124.91, 124.58, 123.97, 123.53, 123.26, 122.63, 118.48, 104.84, 75.10, 74.82, 44.56, 31.83, 30.44, 28.93, 25.86, 22.79, 14.35, 14.09. MS: *m/z* 664.16 [M^+]. Anal. Calcd. for $C_{32}H_{43}BrN_2O_2S_3$: C, 57.90; H, 6.53. Found : C, 57.54 ; H, 6.38.

(5'-Hexyl-2,2'-bithiophen-5-yl)-5,6-bis(hexyloxy)benzo[c][1,2,5]thiadiazole-*(4,5-(Di-2-ethylhexyl)-dithieno) [2,3-d:2′,3′-d′]thieno[3,2-b:4,5-b′]dipyrrole (K).*

4,5-(Di-2-ethylhexyl)-2,7-bis(trimethylstannyl)-dithieno[2,3-d:2′,3′-d′]thieno[3,2-b:4,5-b′] dipyrrole (**1**) (0.42 g, 0.5 mmol), 4-bromo-7-(5'-hexyl-2,2'-bithiophen-5-yl)-5,6-bis(hexyloxy) benzo[c][1,2,5]thiadiazole (**3**) (1.52 g, 2.2 mmol)toluene (15 mL) were all added into a double-necked round-bottomed flask. The reaction container was de-aerated with argon for 5 min followed by the addition of $Pd(PPh_3)_4$ (0.03 g, 0.02 mmol) and de-aeration for another 20 min with argon to remove O_2. After being heated to reflux for 16 h at 110 °C, the reaction mixture was cooled down to room temperature, poured into water and extracted with CH_2Cl_2. The solvent was removed by rotary evaporation, and the crude product was purified by flash column chromatography on silica gel using a mixture of chloroform and hexane (1 : 2) as eluent. Finally, evaporation of the solvent afforded the targeted compound (**K**), as a dark navy powder. Yield: 61%

^{1}H NMR (300 MHz, $CDCl_3$): δ 8.78 (s, 2H), 8.47 (d, 2H, J = 4.2 Hz), 7.23 (d, 2H, J = 3.3 Hz), 7.11 (d, 2H, J = 3.3 Hz), 6.74 (d, 2H, J = 3.6 Hz), 4.42 (dd, 4H, J = 6.0 Hz), 4.22 (dd, 8H, J = 7.5 Hz), 2.84 (dd, 4H, J = 7.5 Hz), 1.98-2.10 (m, 10H), 1.70 (m, 4H), 1.25-1.39 (m, 52H), 0.81-0.93 (m, 30H). ^{13}C NMR (75 MHz, $CDCl_3$): δ 152.07, 151.48, 151.28, 151.14, 146.17, 145.88, 139.61, 135.50, 133.41, 132.31, 132.10, 131.82, 124.73, 123.72, 119.05, 118.16, 116.82, 115.83, 74.87, 41.37, 32.54, 32.34, 31.03, 30.87, 30.63, 30.45, 29.55, 26.45, 23.53, 21.34, 14.80, 11.83. MS: *m/z* 1663.70 [M^+]. Anal. Calcd. for $C_{92}H_{122}N_6O_4S_9$: C, 66.38;

H, 7.39. Found : C, 66.02 ; H, 7.18.

Device fabrication and characterization

The small molecule BHJ organic solar cells were fabricated with the configuration of ITO coated glass /PEDOT: PSS/**J** or **K**:$PC_{71}BM$/Al by using a conventional solution spin coating method. Firstly, the indium tin oxide (ITO) coated glass substrates were cleaned subsequently by ultrasonic treatment in detergent, deionized water, acetone and isopropyl alcohol for 20 min. A layer of PEDOT:PSS was spinnings coated (3500 rpm, ~40 nm) onto ITO coated glass substrate and baked at 120° C for 20 min. The active layer was spin coated onto the top of PEDOT:PSS layer from the different weight ratios of **J** or **K** and $PC_{71}BM$ in dichlorobenzene (DCB) at 1500 rpm for 25s. For two steps annealing (TSA) treatment, first the optimized active blended layer was thermal annealing (TA), by placing the active layer on hot plate at 110° C for 5 min and then cooled up to room temperature. The active layer was placed in a glass Petri dish containing 200 μL THF for 5 min for subsequent solvent vapor annealing. The thickness of the active layers is about 80 ±5 nm. Finally 50 nm aluminum (Al) layer was deposited onto the top of the active layer under the high vacuum by a shadow mask. The effective area of each device is about 20 mm^2. The hole-only and electron-only devices with ITO/PEODT:PSS/active layer/Au and ITO/Al/active layer:$PC_{71}BM$/Al architectures were also fabricated in an analogous way in order to measure the hole and electron mobility, respectively. The current–voltage characteristics of BHJ organic solar cells were measured using a computer controlled Keithley 238 source meter under simulated AM 1.5G, 100 mW/cm^2. A xenon light source coupled with optical filter was used to give the stimulated irradiance at the surface of the devices. The incident photon to current efficiency (IPCE) of the devices was measured at illuminating the device through the light source and monochromator and the resulting current was measured using a Keithley electrometer under short circuit condition.

Results and discussion

Synthesis of materials

We have synthesized two A-D-A type small molecules, J and **K** based on S, N heteropentacene donor central core unit and different acceptors according to the synthetic route as shown in scheme 1. These molecules were characterized by ^1H NMR and ^{13}C NMR spectroscopy as described in experimental parts.

Optical and electrochemical properties

The optical absorption spectra of **J** and **K** in chlorobenzene (CB) and spin cast from the CB solution are shown in Figure 1 and the data are summarized in Table 1. Small molecules, **J** and **K** showed strong intramolecular charge transfer (ICT) absorption bands at 650 nm and 629 nm, respectively, with high molar extinction coefficients (ε) by 84482 M^{-1} cm^{-1} and 77765 $M^{-1}cm^{-1}$ for **J** and **K**, respectively. The red shift of 21 nm and higher ε for **J** compared to **K** can be ascribed to the stronger electron accepting ability of un-substituted BT compared to alkoxy substituted BT. In addition to ICT bands, both **J** and **K** showed absorption bands in the short wavelength region around 400-410 nm, ascribed to characteristics π-π* transition of the conjugated backbone. In comparison, of the solution, absorption spectra in thin film showed significant broadening and the absorption maxima assigned to ICT band is redshifted compared to that measured in solution, attributed to the increased intermolecular interactions of the molecules in the solid state. The vibronic shoulder observed might arise from better molecular packing in solid state.[48] The optical bandgaps (E_g^{opt}) for **J** and **K** estimated from the onset absorption spectra in thin film were about 1.52 eV and 1.60 eV, respectively. These values are lower that the $E_{o\text{-}o}$ (Figure 2b) estimated from the intersection of absorption and emission spectra of molecules in solution (1.68 eV and 1.77 eV for **J** and **K**, respectively).

We have estimated the HOMO energy level from the cyclic voltammetry of these small molecules in the film (Figure 2a). The electrochemical parameters are summarized in Table 1. The HOMO energy level was deduced from the oxidation onset with the assumption that the energy level of ferrocene is 4.8 eV below the vacuum level. But the reduction potential of these was not clearly observed in the cyclic voltammogram. Therefore, we have determined the $E_{o\text{-}o}$ transition energy from the intersection of the absorption and emission spectra of **J** and **K** in solution (Figure 3). The HOMO energy level of **J** and **K**, estimated from the onset oxidation potential observed in CV was-5.09 eV and -5.12 eV, respectively. The deeper HOMO energy level is beneficial for a high value of V_{oc}, when used as the donor for the fabrication of BHJ solar cells along with $PC_{71}BM$ as the electron acceptor. The LUMO energy level was estimated according $E_{LUMO} = E_{HOMO} - E_{o\text{-}o}$ and was about -3.41 eV and -3.35 eV for **J** and **K**, respectively. In general, an exciton dissociation and efficient electron transfer from the donor to the acceptor molecule requires a higher LUMO level of the donor by at least ~0.3 eV compared to the LUMO energy level of the acceptor molecule.[49,50] The LUMO level of the $PC_{71}BM$ has values in the range between 3.9 eV to 4.1 eV.[51] In our case, the LUMO–LUMO offset between **J** or **K** and $PC_{71}BM$ is larger than 0.3 eV, expecting that

the exciton might easily dissociate at the donor–acceptor interface formed in the BHJ active layer.

Density Functional Theory (DFT)

Optimized structures were calculated by TD-DFT using the B3LYP functional and the 6-21G* basis set. The highest occupied molecular orbital (HOMO) and the lowest unoccupied molecular orbital (LUMO) energies were determined using minimized singlet geometries to approximate the ground state. Isodensity surface plots of **J** and **K** calculated by the time dependent-density functional theory (TD-DFT) using the B3LYP functional/6-31G*basis set are shown in Figure 3. The HOMO level of both **J** and **K** were predominated located at S, N heteropentacene whereas LUMO level of **J** and **K** was located at un-substituted and alkoxy substituted benzothiadiazole (BT), respectively. The theoretical values of HOMO and LUMO energy levels are compiled in Table 1 and are consistent with the experimentally observed values.

.Photovoltaic properties

Bulk heterojunction organic solar cells were fabricated using **J** and **K** as electron donors along with $PC_{71}BM$ as electron acceptor with a device structure ITO/PEDOT:PSS/**J** or **K**:$PC_{71}BM$/Al, using conventional spin coating method for BHJ active layer deposition. The concentration ratio of the donor and acceptor in the blended active layer is important for the photovoltaic performance of the device, since there should be a balance between the absorption of active layer and charge transport of the carriers towards the electrodes. We have used different concentration in weight ratio of donor and acceptor and found that the 1:1 w/w ratio exhibits the best power conversion efficiency. The current-voltage (J-V) characteristics of the organic solar cells with an optimized active layer cast from CB are shown in Figure 4a and 5a, for **J**:$PC_{71}BM$ and **K**:$PC_{71}BM$ active layers, respectively and corresponding photovoltaic parameters are complied in table 2. The optimized solar cell as cast **J**:$PC_{71}BM$ blend film showed a PCE of 1.96 % with open V_{oc} of 0.86 V, J_{sc} of 6.52 mA/cm^2 and FF of 0.36. The corresponding solar cell based on **K**:$PC_{71}BM$ exhibit the PCE of 1.57% with V_{oc} of 0.88 V, J_{sc} of 5.58 mA/cm^2 and FF of 0.32. The similar V_{oc} of both devices could be attributed to the similar values of HOMO energy levels of **J** and **K** small molecules. The relatively high value of J_{sc} for device based on **J** may be attributed to a broader absorption profile of the **J**:$PC_{71}BM$ film (Figure 6) as compared to **K**:$PC_{71}BM$. The low values of J_{sc} and FF for these devices may be attributed to the un-optimized morphology of the active layers, which will be discussed in the later part of the discussion.

In order to improve the PCE of the devices, first we adopted the thermal annealing (110° C for 10 min) of the active layer and found that the devices based on J:PCBM (1:1) and K:PC71BM (1:1) showed PCE of 2.78 % and 2.14 %, respectively. We have also fabricated the devices using the solvent vapor annealing treatment of active layer and the PCE of 4.14 % and 3.77 % was achieved for J:$PC_{71}BM$ and K:$PC_{71}BM$ based devices, respectively. It was reported that a simple two step annealing (TSA) approach that combined thermal annealing and solvent vapor annealing can improved to morphology of the active layer[52,53] to improve the PCE. Herein, we have also employed same approach for the optimization of morphology of active layer in order to improve the PCE. The device based on **J**:$PC_{71}BM$ and **K**:$PC_{71}BM$ with TSA treatment showed PCE of 6.02 % (J_{sc} = 11.13 mA/cm^2, V_{oc} = 0.82 V and FF= 0.66) and 5.06 % (J_{sc}= 9.88 mA/cm^2, V_{oc} =0.84 V and FF= 0.61), respectively.

The IPCE spectra of the devices based on **J** and **K** small molecules as donors are shown in Figure 4b and 5b, respectively. As shown in Figure 4b and 5b, the devices fabricated with both **J**:$PC_{71}BM$ and **K**:$PC_{71}BM$ blend films (as cast) showed relatively low IPCE (maximum IPCE values are 38 % and 32 % for **J** and **K**, respectively). After TSA treatment, the IPCE of the devices based on **J**:$PC_{71}BM$ and **K**:$PC_{71}BM$ was significantly improved with maximum values of 54 % and 43 %, respectively. Moreover, IPCE spectra of TSA treated devices exhibited a red shift in the response. The J_{sc} values estimated from the integration of IPCE spectra for these devices were also complied in table 2 which are consistent with the experimentally observed values. However, a slight decrease in V_{oc} of devices based on TSA treated active layers may be due to the increasing intermolecular interaction between donor and acceptors, as evidenced from the increased values of R_{sh} compared to the devices based on cast active layers.[54, 55]

As overall PCE of the solar cell depends upon the light absorption and charge transport properties of the active layer used in the corresponding device; we have investigated the change in these parameters with and without TSA treatment. As shown in Figure 6a and 6b, the blended films with TSA showed the red-shift absorption as well as a higher absorption coefficient, which is consistent with the red-shift in the IPCE spectra. Moreover, the blended films of either **J** or **K** with $PC_{71}BM$ without TSA exhibit a blue shift absorption peak, indicating that the mixing of $PC_{71}BM$ disrupts the intermolecular packing of donor molecules. After the TSA treatment, the absorption peaks in the blended film are red-shifted relative to cast film and also exhibit an increasing shoulder peak. These suggest that better molecular ordering is formed for donor molecules in the corresponding blended films after TSA

treatment. In addition, the presence of strong donor also demonstrates the better ordering of **J** and **K** in their respective blends after TSA treatment. The broader absorption profile and higher absorption coefficient of TSA treated blend films could increase the exciton generation efficiency, leading to an increase in J_{sc} and PCE.

To get information about the molecular ordering induced by the TSA, the change in microstructures of the donor in blends was investigated by X-ray diffraction. The thin film of both pure **J** and **K** showed a strong (100) diffraction peak at 2θ=5.23° and 5.20°, respectively (Figure 7a), corresponding to the d-spacing of 2.24 nm and 2.15 nm, respectively between the molecular layers indicating that the different acceptor units had a slight effect on the crystal dimension. The XRD pattern of as cast and TSA treated **J**:$PC_{71}BM$ films are shown in Figure 7b. Similar XRD patterns were also observed in **K**:$PC_{71}BM$ films. As the cast blend film showed relatively broad and weak (100) diffraction peak at 2θ=5.23°, corresponding to the d-spacing of 2.16 nm between the molecular layer of J. However, in the TSA treated film, the (100) diffraction peak slightly to 2θ= 5.26° and also becomes narrower and intense. As seen from the FWHM value, and more intense, indicating the increase in the crystalline nature of the active layer. The increase in the crystalline nature of active layer also leads to improve the molecular packing. Moreover, the shifting of (100) diffraction peak toward higher 2θ also indicated the denser molecular packing. The overall increase in the order of the molecular packing improves the IPCE values likely to the responsible for the increase in the J_{sc} and PCE.

The transmission electron microscopy studies show that the morphologies of as cast and TSA treated blend thin films are quite different (Figure 8). Without TSA, both blended films show no indication of phase separation between donor and acceptor which is not favorable for efficient charge transport, thus leading to low J_{sc} and FF. When the blended films are subjected to TSA treatment, the film exhibits clear phase separating interpenetrating network with domain sizes of 25-30 nm, which is comparable to the exciton diffusion length.[56, 57] The TSA treatments may redistribute the donor and acceptor phases in the active layers to form the optimal phase separation by increasing the molecular ordering and crystallization. The improved phase separation and morphology of the active layers with TSA treatment may increase the exciton dissociation and charge transport and suppress the charge carrier recombination, resulted increase in J_{sc} and FF.

To check the effect of TSA treatment on the charge transport in devices, the space charge limited current (SCLC) method was employed to estimate the hole mobility with a hole only device (ITO/PEDOT:PSS/**J** or **K**:$PC_{71}BM$/Al. The SCLC can be fitted by the Mott-

Gurney expression: $J = (9/8)\ \varepsilon_o\varepsilon_r\mu(V^2/d^3)$[58], where J is dark current density, ε_r is the relative dielectric constant of the active layer, and ε_o is the free-space permittivity ($8.85\text{x}10^{-12}$ F/m), d is the thickness of the active layer, $V= V_{appl}-V_{bi}$, where V_{appl} is the applied voltage and V_{bi} is the V_{bi} is the built-in potential that results from the difference in the work function of the anode and cathode. Figure 9 shows the J-V characteristics of the hole only devices for **J**: $PC_{71}BM$ and **K**: $PC_{71}BM$ blends with and without TSA treatment. For the devices as cast blend film, the hole mobilities are $5.68\ \text{x}10^{-5}$ cm^2/Vsand $2.32\text{x}10^{-5}$ cm^2/Vs for **J**: $PC_{71}BM$ and **K**:$PC_{71}BM$, respectively. After TSA treatment, the hole mobilities are improved up to 1.45 $\text{x}10^{-4}$ cm^2/Vs and 7.65 $\text{x}10^{-5}$ cm^2/Vs for **J**:$PC_{71}BM$ and **K**:$PC_{71}BM$, respectively. The increase in the hole mobility may be attributed to the increase in the crystallinity of the active layer. The electron mobilities for as cast in **J**:$PC_{71}BM$ and **K**:$PC_{71}BM$ are about $3.45\ \text{x}\ 10^{-4}$ cm^2/Vs and $3.40\ \text{x}\ 10^{-4}$ cm^2/Vs, respectively. However, the electron mobilities do not change much, i. e. $3.52\ \text{x}\ 10^{-4}$ cm^2/Vs and $3.46\ \text{x}10^{-4}$ cm^2/Vs for **J**:$PC_{71}BM$ and **K**:$PC_{71}BM$, respectively, after the TSA treatment. Therefore the improved and the more balanced electron to hole mobilities in blended films after TSA treatment may promote the charge transport and suppress the charge recombination, resulting in the enhancement in the PCE.

To get further information about the effect of TSA on the charge generation and extraction processes, the variation of photocurrent (J_{ph}) with internal voltage of the devices was investigated. The photocurrent (J_{ph}) is the difference between the current under illumination (J_L) and dark current (J_D), i.e. $J_{Ph}= J_L-J_D$. The J_{ph} can be expressed as $J_{ph} = qLG_{max}$ P_c, where L is the thickness of the active layer, G_{max} is the maximum generation rate for electron-hole pairs and P_c is the charge collection probability.[59-61] In any solar cell upon illumination, the photoactive layer absorbs solar photons and generates excitons, which undergo dissociation at D/A interfaces, forming bound e-h pairs. The bound e-h pairs are separated into free charge carriers and then drifted toward different electrodes under the drive of internal field. The internal effective field is defined as $V_{eff} = V_o-V_{appl}$, where V_o is the voltage at which J_{ph} is zero and V_{appl} is the applied voltage. The variation of J_{ph} with internal voltage V_{eff} is shown in Figure 10. The log-log plot of J_{ph} versus V_{int} shows two distinct regions: a linear region and a saturation region, where J_{ph} was saturated at $V_o-V_{appl} >0.52$ V for devices based on TSA treated active layers. The field independent saturation region suggests the negligible trapped charges and efficient charge extraction and collection. On the other hand, the devices based on the active layers without TSA treatment showed no clear saturation in J_{ph} with increasing V_{int}, indicating significant electron-hole recombination,

where a stronger internal electric field is needed to sweep out the photogenerated charge carriers and separate the germinate electron-hole pairs.[62] This is closely related to the film morphology of active layer with TSA, which hinders efficient charge transport. In addition, the photogenerated J_{ph} of TSA treated devices were higher than that of devices without TSA, suggesting higher charge generation and charge extraction. The values of G_{max} can be calculated by $J_{phsat} = qG_{max}L$. The increase in the value of G_{max} for TSA treated devices suggests that the treatment of TSA amplifies the exciton generation rate, which is a measure of the number of photons absorbed.[63,64] These results are consistent with the absorption profile and morphology of active layers and photovoltaic performance of the devices. To get information about the exciton dissociation efficiency and charge collection efficiency, the ratio of J_{sc}/ J_{phsat} was estimated[65] to be 0.59, 0.83, 0.53 and 0.78 for **J**:$PC_{71}BM$ (as cast), **J**:$PC_{71}BM$ (TSA) **K**:$PC_{71}BM$ (as cast) and **K**:$PC_{71}BM$ (TSA) active layers. The greater values of this ratio for the devices processed with TSA treatment are attributed to the better phase separation in the active layer, increased hole mobility, improved balanced charge transport and enhancement in the light harvesting ability. All these parameters demonstrate that TSA improves the exciton dissociation efficiency, and charge transport and collection efficiency, and also reduces the carrier recombination.

Conclusions

In summary, we have designed and synthesized two new A-D-A small molecules with same electron rich planar S, N heteropentacene central core flanked with alkoxy substituted and un-substituted benzothiadiazole (BT) acceptor units by end capped with hexyl-substituted bi-thiophene units and investigated their optical and electrochemical properties. The devices based on optimized active layers **J**:$PC_{71}BM$ and **K**:$PC_{71}BM$ processed from CB solvent exhibit overall PCE of 1.96 % and 1.57 %, respectively. The higher PCE of former device is attributed to its broader absorption profile and larger hole mobility compared to that of the later. The overall PCE has been improved up to 6.06 % and 5.02 % of these devices, when TSA treatment of active layers was employed. The enhancement in the PCE has been attributed to the increased value of J_{sc} and FF. The morphological investigation demonstrated that higher valves of J_{sc} and FF were attributed to suitable phase separation between donor and acceptor, increased light harvesting efficiency, higher exciton dissociation efficiency of more balanced charge transport and reduced charge recombination induced by the TSA treatment of active layers.

Acknowledgement

This work was supported in part by the National Research Foundation of Korea (NRF) grant funded by Korea Government (MSIP) (2014R1A2A2A03004716). GDS thanks to the management, JEC group of colleges, Jaipur Engineering College, Jaipur for providing necessary support.

References

1. Y. Su, S. Lan, and K. Wei, *Mater. Today* 2012, **15**, 554-562.
2. R. A. J. Janssen and J. Nelson, *Adv. Mater*. 2013, **25**, 1847-1858.
3. S. Lizin, V. Passel, E. De Schepper, W. Maes, L. Lutsen, J. Manca and D. Vanderzande, *Energy Environ. Sci.* 2013, **6**, 3136-3149.
4. L. Ye, S. Zhang, L. Hu, M. Zhang and J. Hou, *Acc. Chem. Res.* 2014, **47**, 1595-1603.
5. K. Mazzio and C. K. Luscombe, *Chem. Soc. Rev.* 2015, **44**, 78-90.
6. A. J. Heeger, *Adv. Mater.* 2014, **26**, 10-28.
7. L. Lu, T. Zheng, Q. Wu, A. M. Schneider, D. Zhao, L. Yu, *Chem. Rev.* doi: 10.1021/acs.chemrev.5b00098.
8. G. Li, R. Zhu and Y. Yang, *Nat. Photonics* 2012, **6**, 153−161.
9. G. Yu, J. Gao, J. Hummelen, F. Wudl and A. J. Heeger, *Science*, 1995, **270**, 1789-1791.
10. J. J. M. Halls, C. A. Walsh, N. C. Greenham, E. A. Marseglia, R. H. Friend, S. C. Moratti and A. B. Holmes, *Nature* 1995, **376**, 498−500.
11. J. D. Chen, C. Cui, Y. Q. Li, L. Zhou, Q. D. Du, C. Li, Y. Li, and J. X. Tang, *Adv. Mater*. 2015, **27**, 1035-1041.
12. Y. Liu, J. Zhao, Z. Li, C. Mu, H. Hu, K. Jiang, H. Lin, H. Ade and H. Yan, *Nat. Commun*. **2014**, *5*, 5293.
13. L. Ye, S. Zhang, W. Zhao, H. Yao and J. Hou, *Chem. Mater.* 2014, **26**, 3603-3605.
14. T. L. Nguyen, H. Choi, S. J. Ko, M. A. Uddin, B. Walker, S. Yum, J. E. Jeong, M. H. Yun, T. J. Shin, S. Hwang, J. Y. Kim and H. Y. Woo, *Energy. Environ. Sci.* 2014, **7**, 3040-3051.
15. C. Liu, C. Yi, K. Wang, Y. Yang, R. S. Bhatta, M. Tsige, S. Xiao and X. Gong, *ACS Appl. Mater. Interfaces* 2015, **7**, 4928−4935
16. J. Roncali, *Acc. Chem. Res.* 2009, **42**, 1719-1730.
17. B. Walker, C. Kim and T. Q. Nguyen, *Chem. Mater*. 2011, **23**, 470-482.
18. Y. Lin, Y. Li and X. Zhan, *Chem. Soc. Rev.* 2012, **41**, 4245- 4272.
19. J. Ronacali, P. Leriche and P. Blanchard, *Adv. Mater*. 2014, **26**, 3821-3838.
20. J. E. Coughlin, Z. B. Henson, G. C. Welch and G. C. Bazan, *Acc. Chem. Res*. 2014, **47**, 257−270.

21. W. Ni, X. Wan, M. Li, Y. Wang and Y. Chen, *Chem. Commun*. 2015, **51**, 4936-4950.
22. M. Li, W. Ni, X. Wan, Q. Zhang, B. Kan and Chen, *J. Mater. Chem. A* 2015, **3**, 4765-4776.
23. A. Mishra and P. Bauerle, *Angew. Chem. Int. Ed.* 2012, **51**, 2020-2067.
24. V. Gupta, A. K. K. Kyaw, D. H. Wang, S. Chand, G. C. Bazan and A. J. Heeger, *Sci. Rep*. 2013, **3**, 1965.
25. B. Kan, Q. Zhang, M. Li, X. Wan, W. Ni, G. Long, Y. Wang, X. Yang, H. Feng and Y. Chen, *J. Am. Chem. Soc.* 2014, **136**, 15529-15532.
26. B. Kan, M. Li, Q. Zhang, F. Liu, X. Wan, Y. Wang, W. Ni, G. Long, Y. Yang, H. Feng, Y. Zuo, M. Zhang, F. Hunag, Y. Cao, T. P. Russell and Y. Chen, *J. Am. Chem. Soc*. 2015, **137**, 3886−3893.
27. Q. Zhang, B. Kan, F. Liu, G. Long, X. Wan, X. Chen, Y. Zuo, W. Ni, H. Zhang, M. Li, Z. Hu, F. Huang, Y. Cao, Z. Liang, M. Zhang, T. P. Russell and Y. Chen, *Nat. Photonics*, 2015, **9**, 35-41.
28. Y. Liu, C. C. Chen, Z. Hong, J. Gao, Y. Yang, H. Zhou, L. Dou, G. Li and Y. Yang, *Sci. Rep.* doi: 10.1038/srep03356.
29. M. Li, F. Liu, X. Wan, W. Ni, B. Kan, H. Feng, Q. Zhang, X. Yang, Y. Wang, Y. Zhang, Y. Shen, T. P. Russell and Y. Chen, *Adv. Mater.* doi: 10.1002/adma.201502645.
30. Y. Huang, E. J. Kramer, A. J. Heeger and G. C. Bazan, *Chem. Rev*. 2014, **114**, 7006-7043.
31. Y. Chen, X. Wan and G. Y. Long, *Acc. Chem. Res.* 2013, **46**, 2645−2655.
32. H. Kast, A. Mishra, G. L. Schulz, M. Urdanpilleta, E. Mena-Osteritz, P. Bäuerle, *Adv. Funct. Mater*. 2015, **25**, 3414-3424.
33. C. Wetzel, A. Mishra, E. Mena-Osteritz, A. Liess, M. Stolte, F. Würthner and P. Bäuerle, *Org. Lett.* 2014, **16**, 362-365.
34. A. Mishra, D. Popovic, A. Vogt, H. Kast, T. Leitner, K. Walzer, M. Pfeiffer, E. Mena-Osteritz and P. Bäuerle, *Adv. Mater.* 2014, **26**, 7217-7223.
35. Y. J. Cheng, J. S. Wu, P. I. Shih, C. Y. Chang, P.C. Jwo, W. S. Kao and C.S. Hsu, *Chem. Mater.* 2011, **23**, 2361-2369.
36. Y. X. Xu, C. C. Chueh, H. L. Yip, F. Z. Ding, Y. X. Li, C. Z. Li, X. Li, W. C. Chen and A. K. Y. Jen, *Adv. Mater.* 2012, **24**, 6356-6361.
37. Y. L. Chen, C. Y. Chang, Y. J. Cheng and C. S. Hsu, *Chem. Mater*. 2012, **24**, 3964-3971.

38. B. C. Schroeder, R. Ashraf, S. Thomas, A. J. P. White, L. Biniek, C. Nielsen, W. Zhang, Z. Huang, P. S. Tuladhar, S. E. Watkins, T. D. Anthopoulos, J. R. Durrant and McCulloch, I. *Chem. Commun*. 2012, **48**, 7699-7701.
39. Z. Fei, R. Ashraf, Z. Huang, J. Smith, R. J. Kline, P. D'Angelo, T. D. Anthopoulos, J. R. Durrant, M. Heeney, and I. McCulloch, *Chem. Commun*. 2012, **48**, 2955-2957.
40. C. A. Tseng, J. S. Wu, T. Y. Lin, W. S. Kao, C. E. Wu, S. L. Hsu, Y. Y. Liao, C. S. Hsu, H. Y. Huang, Y. Z. Hsieh and Y. J. Cheng, *Chem. - Asian J*. 2012, **7**, 2102-2110.
41. R. S. Ashraf, B. C. Schroeder, H. A. Bronstein, Z. Huang, S. Thomas, R. J. Kline, C. J. Brabec, P. Rannou, T. D. Anthopoulos, J. R. Durrant and I. McCulloch, *Adv. Mater.* 2013, **25**, 2029-2034.
42. J. A. Love, I. Nagao, Y. Huang, M. Kuik, V. K. Gupta, C. J. Takacs, J. E. Coughlin, L. Qi, T. S. van der Poll, E. J. Kramer, A. J. Heeger, T. Q. Nguyen and G. C. Bazan, *J. Am. Chem. Soc.* 2014, **136**, 3597-3606.
43. C. Steck, M. Franckevicius, S. M. Zakeeruddin, A. Mishra, P. B¨auerle and M. Gr¨atzel, *J. Mater. Chem. A* 2015, **3**, 17738-17746.
44. K. Parab, k. Venkatasubbaiah and F. Jäkle, *J. Am. Chem. Soc.* 2006, **128**, 12879-12885.
45. W. Yong, M. Zhang, X. Xin, Z. Li, Y. Wu and X. Guo and J. Hou, *J. Mater. Chem. A* 2013, **1**, 14214-14220.
46. T. S. van der Poll, J. A. Love, T. Q. Nguyen and G. C. Bazan, *Adv. Mater.* 2012, **24**, 3646–3649.
47. M. Helgensen, S. A. Gevorgyan, F. C. Krebs and R. A. J. Janssen, *Chem. Mater.* 2009, **21**, 4669-4675.
48. M. C. Yuan, M. Y. Chiu, S. P. Liu, C. M. Chen and K. H. Wei, *Macromolecules* 2010, **43**, 6936−6938.
49. C. J. Brabec, C. Winder, N. S. Sariciftci, J. C. Hummelen, A. Dhanabalan, P. van Hal and R. A. J. Janssen, *Adv. Funct. Mater*. 2002, **12**, 709–712.
50. G. Zhao, G. Wu, C. He, F. Q. Bai, H. Xi, H. X. Zhang and Y. Li, *J. Phys. Chem. C* 2009, **113**, 2636-2642.
51. R. Zhou, Q. D. Li, X. C. Li, S. M. Lu, L. P. Wang, C. H. Zhang, J. Huang, P. Chen, F. Li, X. H. Zhu, W. C. H. Choy, J. Peng, Y. Cao and X. A. *Dyes Pigm.* 2014, **101**, 51-57.
52. W. Ni, M. Li, X. Wan, H. Feng, B. Kan, Y. Zuo and Y. Chen, *RSC Adv.* 2014, **4**, 31977−31980.
53. W. Ni, M. Li, F. Liu, X. Wan, H. Feng, B. Kan, Q. Zhang, H. Zhang and Y. Chen, *Chem. Mater*. **2015**, *27*, 6077-6084.

54. C. W. Schlenker and M. E. Thompson, *Chem. Commun.* 2011, **47**, 3702-3716.
55. K. Vandewal, K. Tvingstedt, A. Gadisa, Q. Inganas and J. V. Manca, *Nat Mater.* 2009, **8**, 904-909.
56. X. Yang, J. Loos, S. C. Veenstra, W. J. H. Verhees, M. M. Wienk, J. M. Kroon, A. A. J. Michels and R. A. J. Janssen, *Nano Lett*. 2005, **5**, 579−583.
57. C. M. Proctor, M. Kuik and T. Q. Nguyen, *Prog. Polym. Sci.* 2013, **38**, 1941- 1960.
58. Y. Liang, D. Feng, Y. Wu, S. T. Tsai, G. Li, C. Ray and L. Yu, *J. Am. Chem. Soc*. 2009, **131**, 7792–7799.
59. J. L. Wu, F. C. Chen, Y. S. Hsiao, F. C. Chen, P. Chen, C. H. Kuo, M. H. Huang and C. S. Hsu, *ACS Nano* 2011, **5**, 959-967.
60. V. D. Mihailetchi, L. J..A. Koster, P. W. M. Blom, C. Melzer, B. de Boer, J. K. J. van Duren and R. A. J. Janssen, *Adv. Funct. Mater*. 2005, **15**, 795-801.
61. V. Podzorov, E. Menard, A. Borissov, V. Kiryukhin, J. A. Rogers and M. E. Gershenson, *Phys. Rev. Lett*. 2004, **93**, 086602.
62. C. M. Proctor, C. Kim, D. Neher, and T. Q. Nguyen, *Adv. Funct. Mater.* 2013, **23**, 3584−3594.
63. V. D. Mihailetchi, H. X. Xie, B. de Boer, L. J. A. Koster and P. W. M. Blom, *Adv. Funct. Mater.* 2006, **16**, 699.
64. V. Shrotriya, Y. Yao, G. Li and Y. Yang, *Appl. Phys. Lett.* 2006, **89**, 063505.
65. Z. He, C. Zhong, X. Huang, W. Y. Wong, H. Wu, L. Chen, S. Su and Y. Cao, *Adv. Mater.* 2011, **2** , 4636-4643

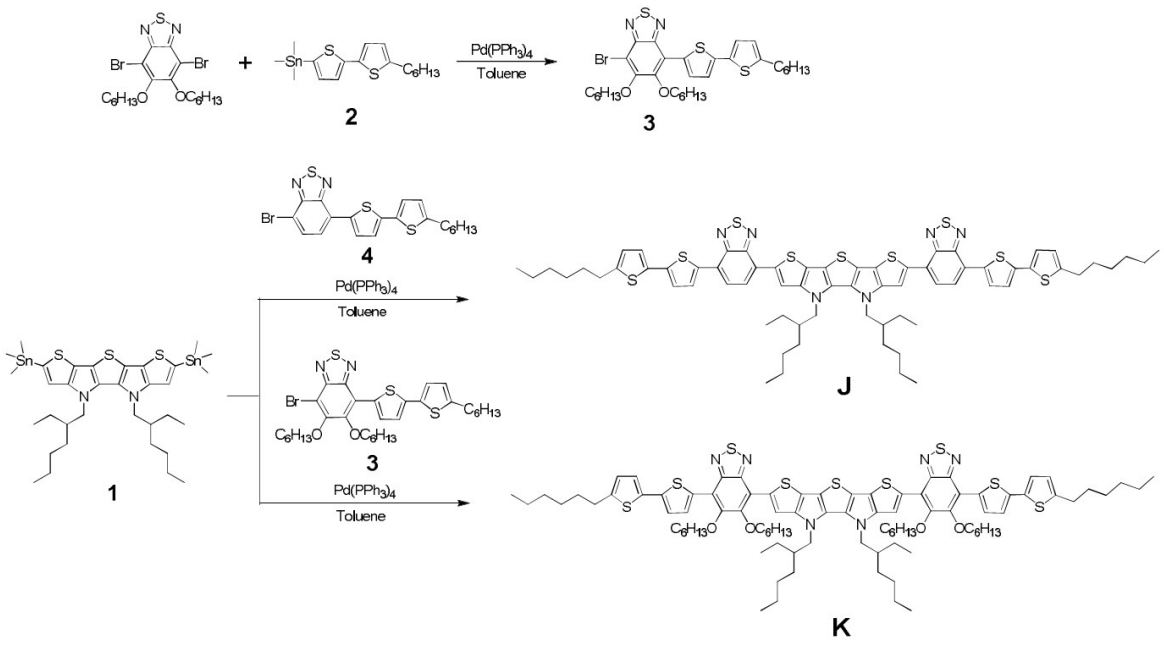

Scheme 1 Synthesis of **J** and **K**

Table 1 Optical and electrochemical parameters of **J** and **K** small molecules

Compounds	λ_{max}[a]/nm (ε/$M^{-1}cm^{-1}$)	λ_{PL}[a]/nm	E_g^{opt} (eV)[b]	E_{o-o} (eV)[c]	E_{HOMO}(eV)	E_{LUMO}(eV)
J	408 (64 477) 650 (84 482	771	1.52	1.68	-5.09[d] -5.11[e]	-3.41[f] -3.43[e]
K	403 (65 682) 629 (77 765)	753	1.60	1.77	-5.12[d] -5.14[e]	-3.35[f] -3.38[e]

[a]UV-vis absorption spectra and fluorescence spectra were measured in Chlorobenzene solution.
[b]calculated from the onset of absorption spectra in thin film.
[c]E_{o-o} was calculated from the absorption thresholds from absorption spectra
[d]calculated from the redox oxidation potential of the compounds were measured in CH_2Cl_2 with 0.1M $(n\text{-}C_4H_9)_4NPF_6$ with a scan rate of 100 mVs^{-1} (*vs*. Fc/Fc^+), E_{HOMO} = -(E_{onset} + 4.8) eV
[e]theoretically calculated value
[f]E_{LUMO}= E_{HOMO} + E_{o-o}

Table 2 Photovoltaic parameters of organic BHJ solar cells based on **J**:$PC_{71}BM$ (1:2) and **K**:$PC_{71}BM$ (1:2) active layers

Active layer	J_{sc} (mA/cm^2)	J_{sc} (mA/cm2)[c]	V_{oc} (V)	FF	PCE (%)	R_s (Ωcm^2)	R_{sh} (Ωcm^2)
J:$PC_{71}BM$[a]	6.52	6.45	0.86	0.35	1.96 (1.88)[d]	48	453
K:$PC_{71}BM$[a]	5.58	5.48	0.88	0.32	1.57 (1.49)[d]	53	412
J:$PC_{71}BM$[b]	11.13	11.18	0.82	0.66	6.02 (5.98)[d]	23	684
K:$PC_{71}BM$[b]	9.88	9.76	0.84	0.61	5.06 (4.97)[d]	28	582

[a]as cast
[b]TSA treatment
[c] estimated from the IPCE spectra
[d] average of 10 devices

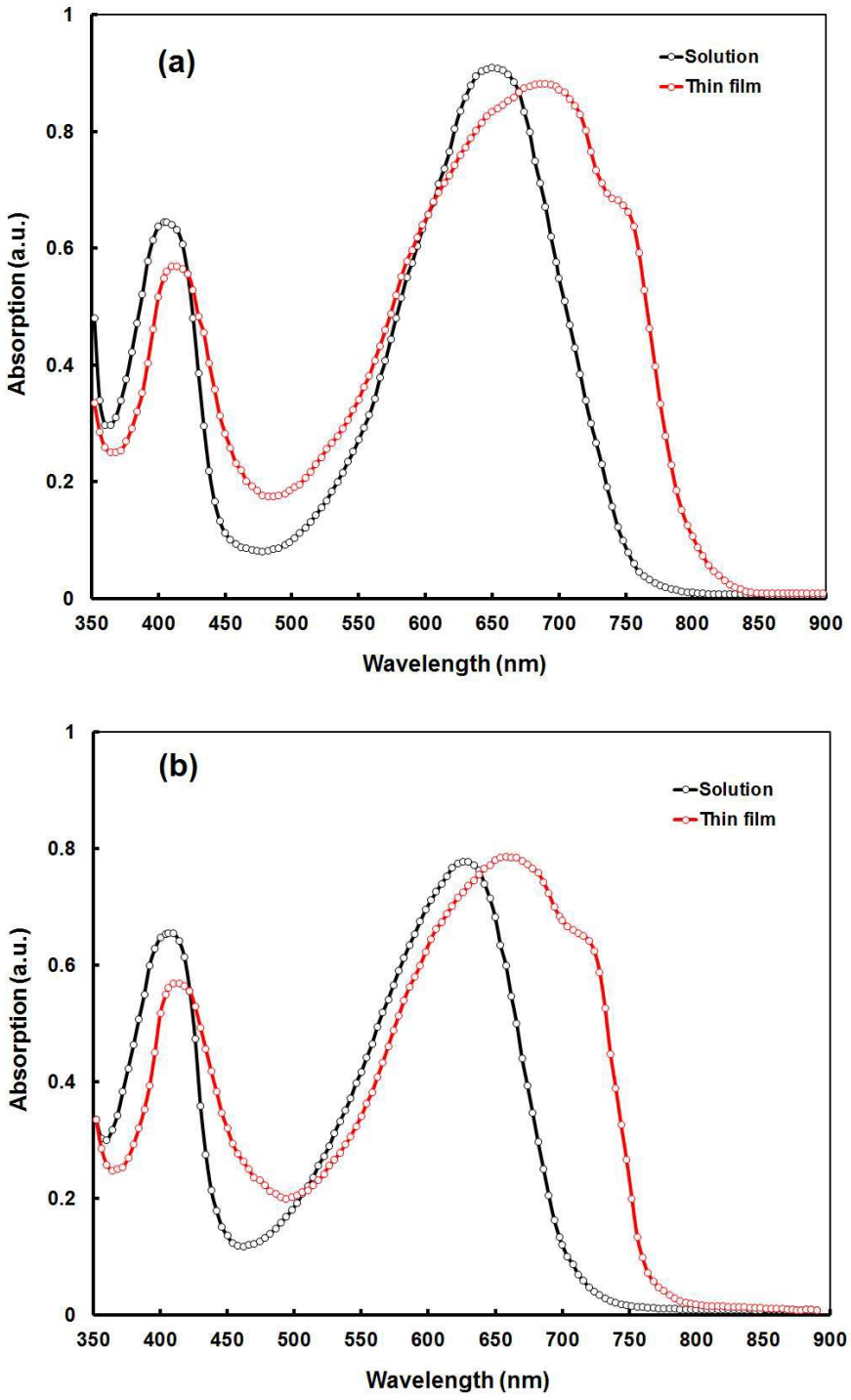

Figure 1 Normalized optical absorption spectra of (a) **J** and (b) **K** in dilute solution (CB) and thin film cast from CB solution

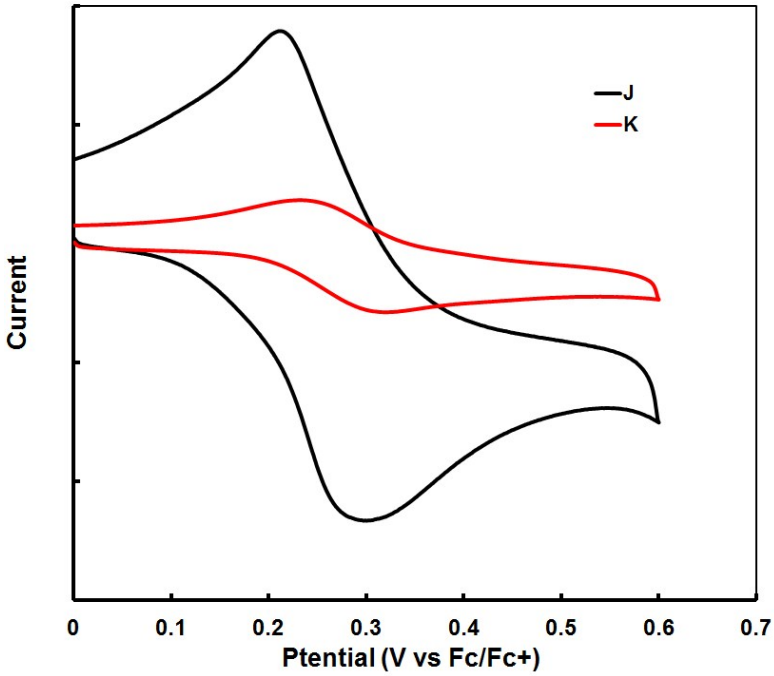

Fig. 2 (a) Electrochemical characterization (oxidation) of the **J** and **K** 0.1 M tetrabutyl ammonium hexafluorophosphate in CH_2Cl_2 at a scan speed of 50 mVs^{-1}, potentials vs.Fc/Fc^{+}.

.

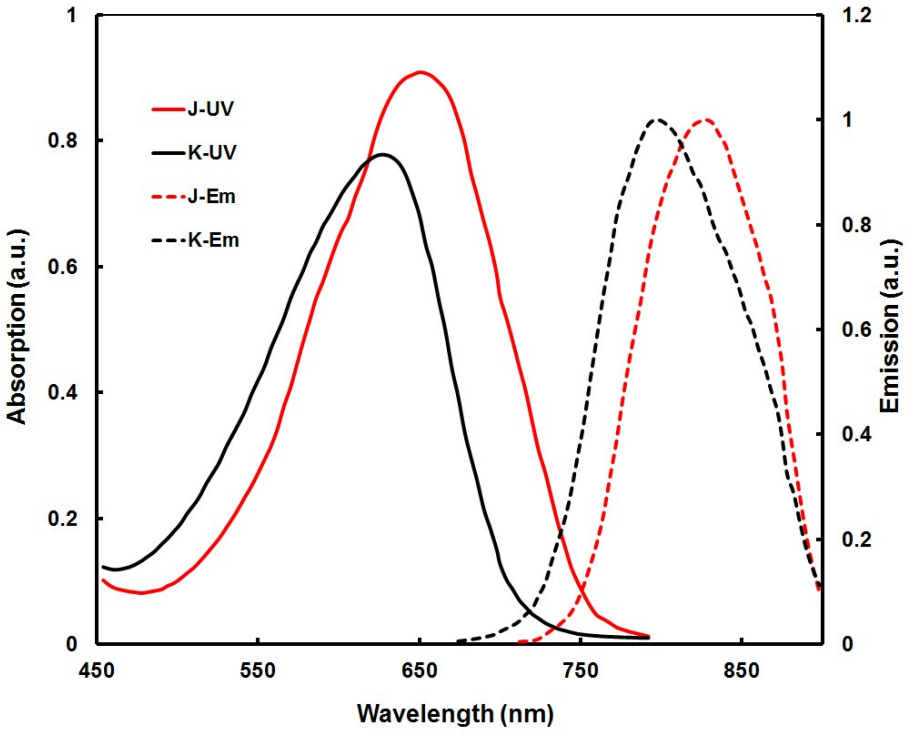

Figure 2 (b) Normalized absorption and emission spectra of **J** and **K** in CB solution.

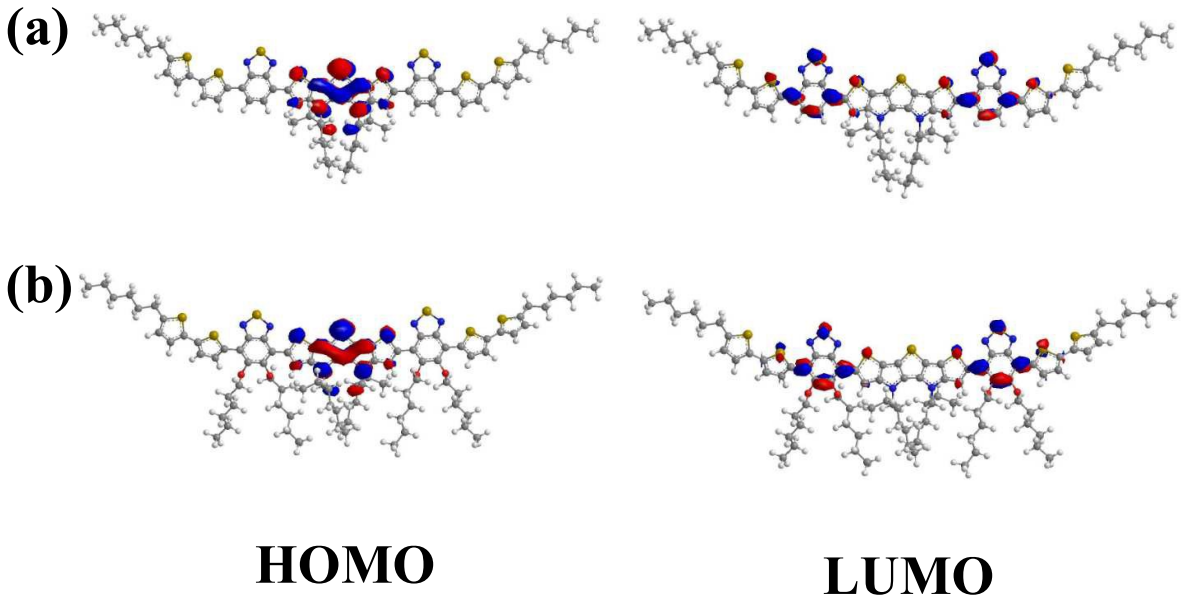

Figure 3 Isodensity surface plots of (a) **J** and (b) **K** calculated by the time dependent-density functional theory (TD-DFT) using the B3LYP functional/6-31G*basis set.

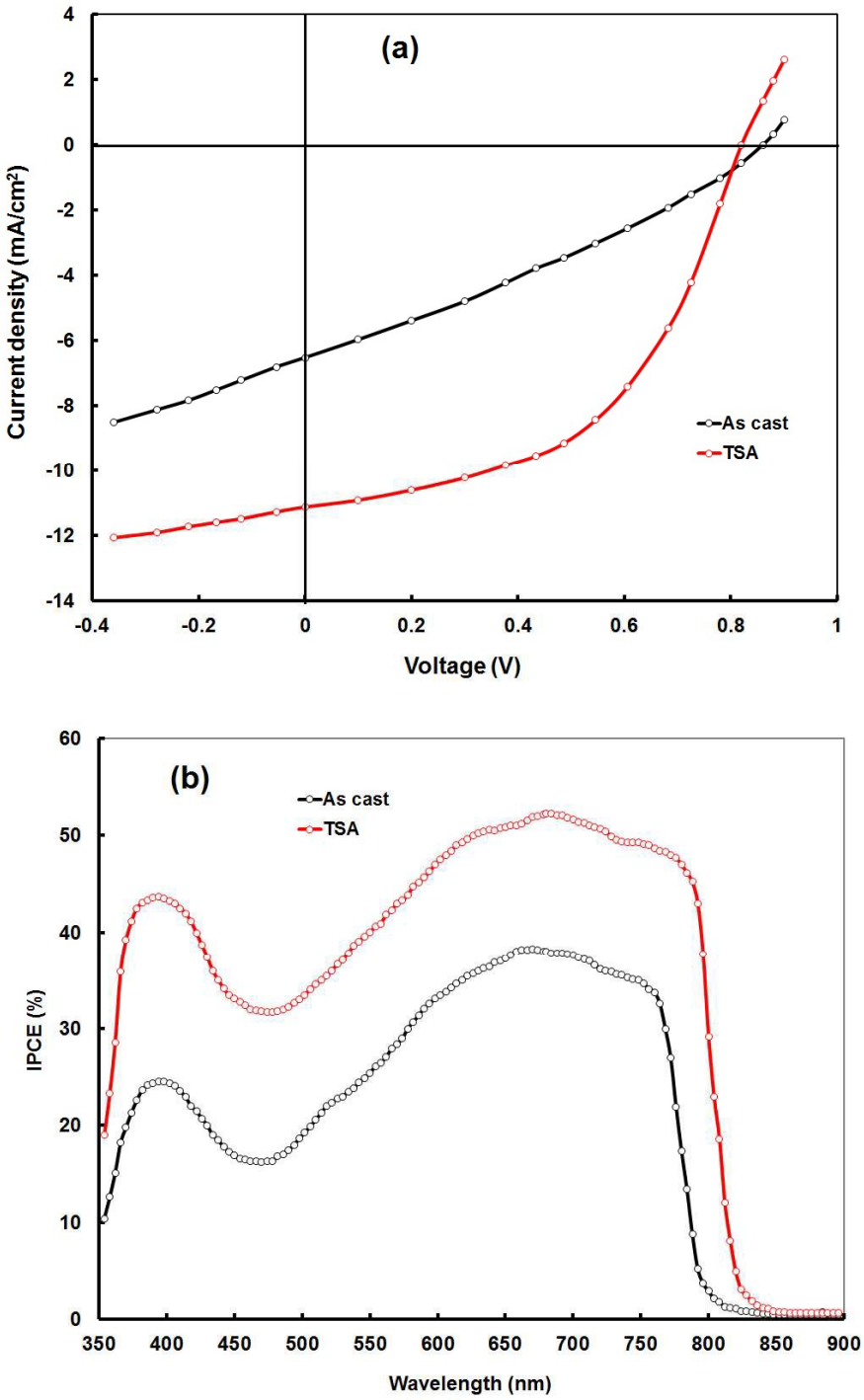

Figure 4 (a) J-V characteristics under illumination and (b) IPCE spectra of optimized **J**:$PC_{71}BM$ active layer (as cast and TSA treatment)

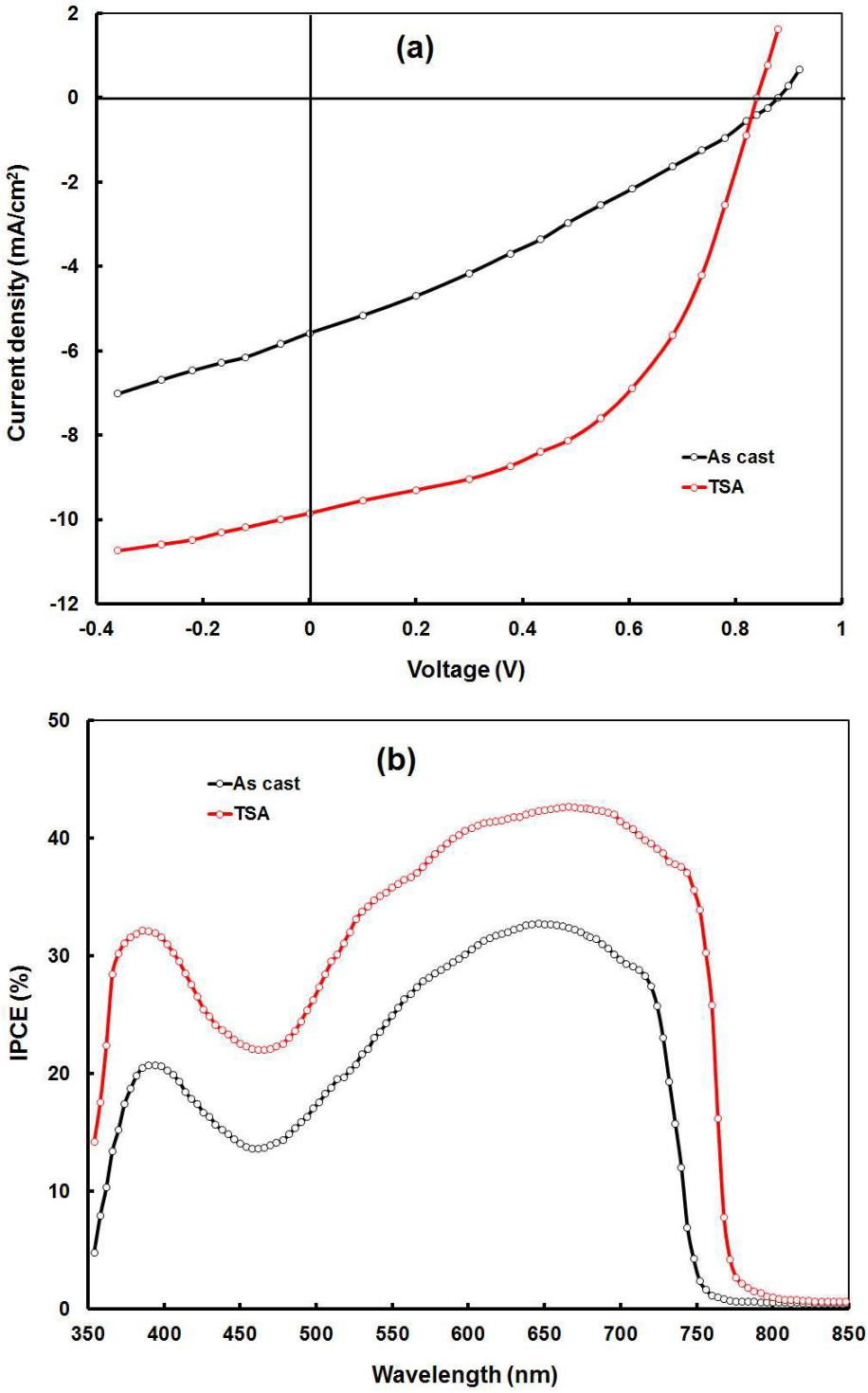

Figure 5 (a) J-V characteristics under illumination and (b) IPCE spectra of optimized **K**:$PC_{71}BM$ active layer (as cast and TSA treatment)

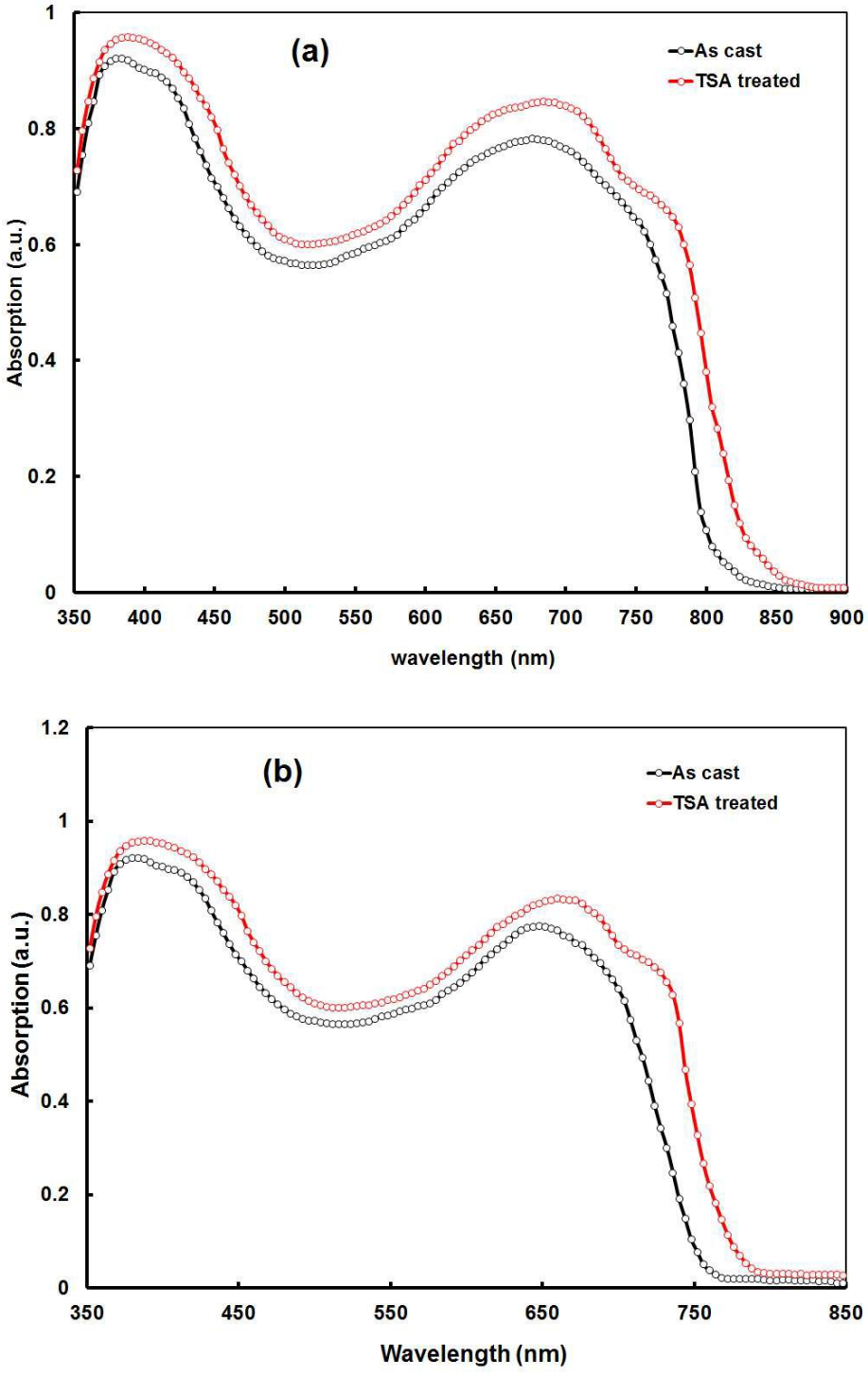

Figure 6 Normalized absorption spectra of optimized (a) **J**:$PC_{71}BM$ and (b) **K**:$PC_{71}BM$ processed with as cast and TSA treatment

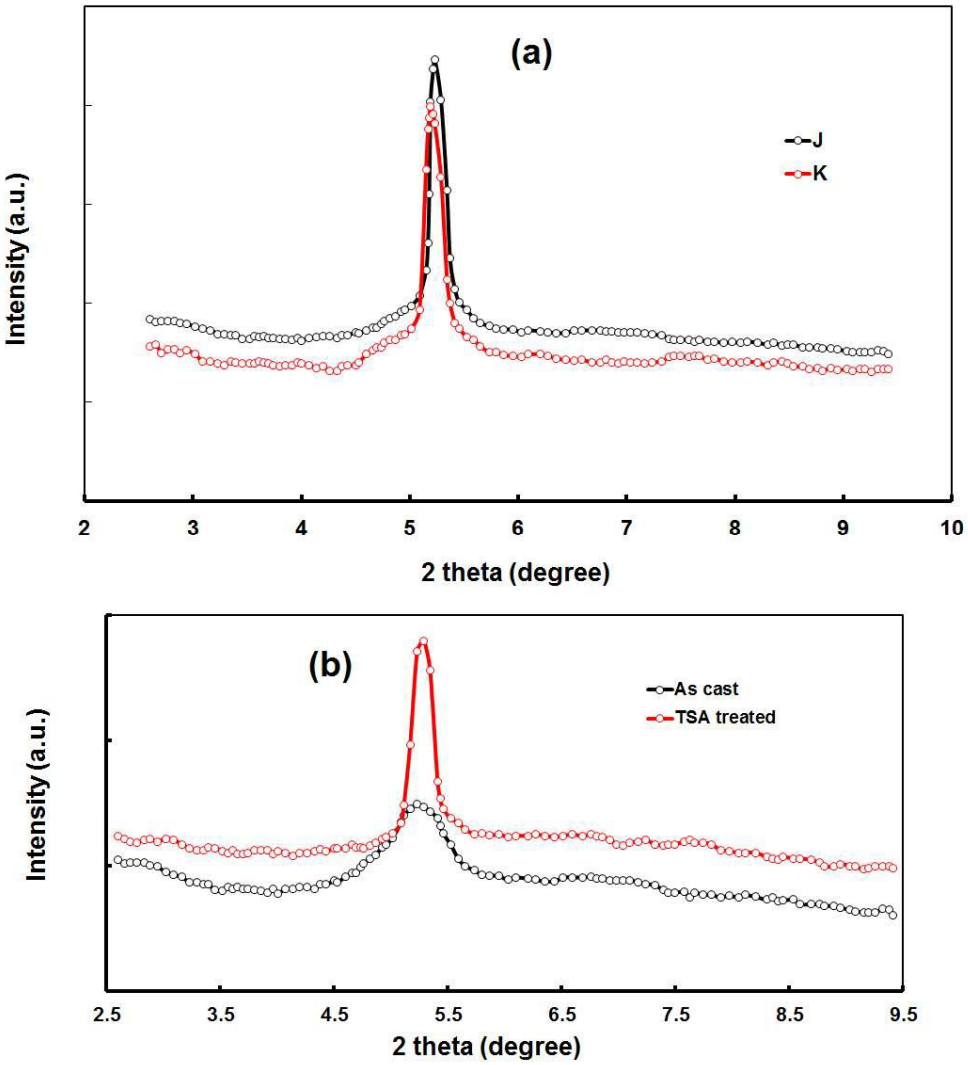

Figure 7 XRD patterns of (a) pristine **J** and **K**, and (b) **J**:$PC_{71}BM$ thin film (as cast and TSA treatment)

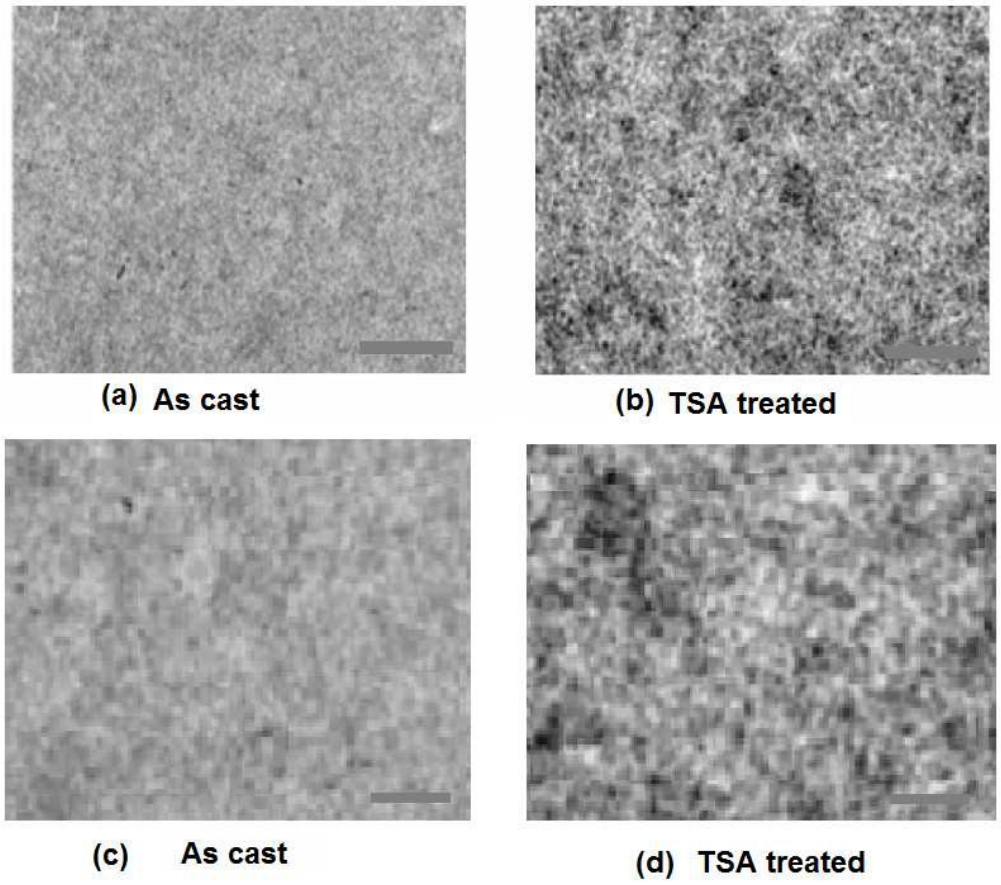

Figure 8 TEM images of (a, b) **J**:$PC_{71}BM$ and (c, d) **K**::$PC_{71}BM$ thin films processed as cast and TSA treatment. Scale bar is 200 nm.

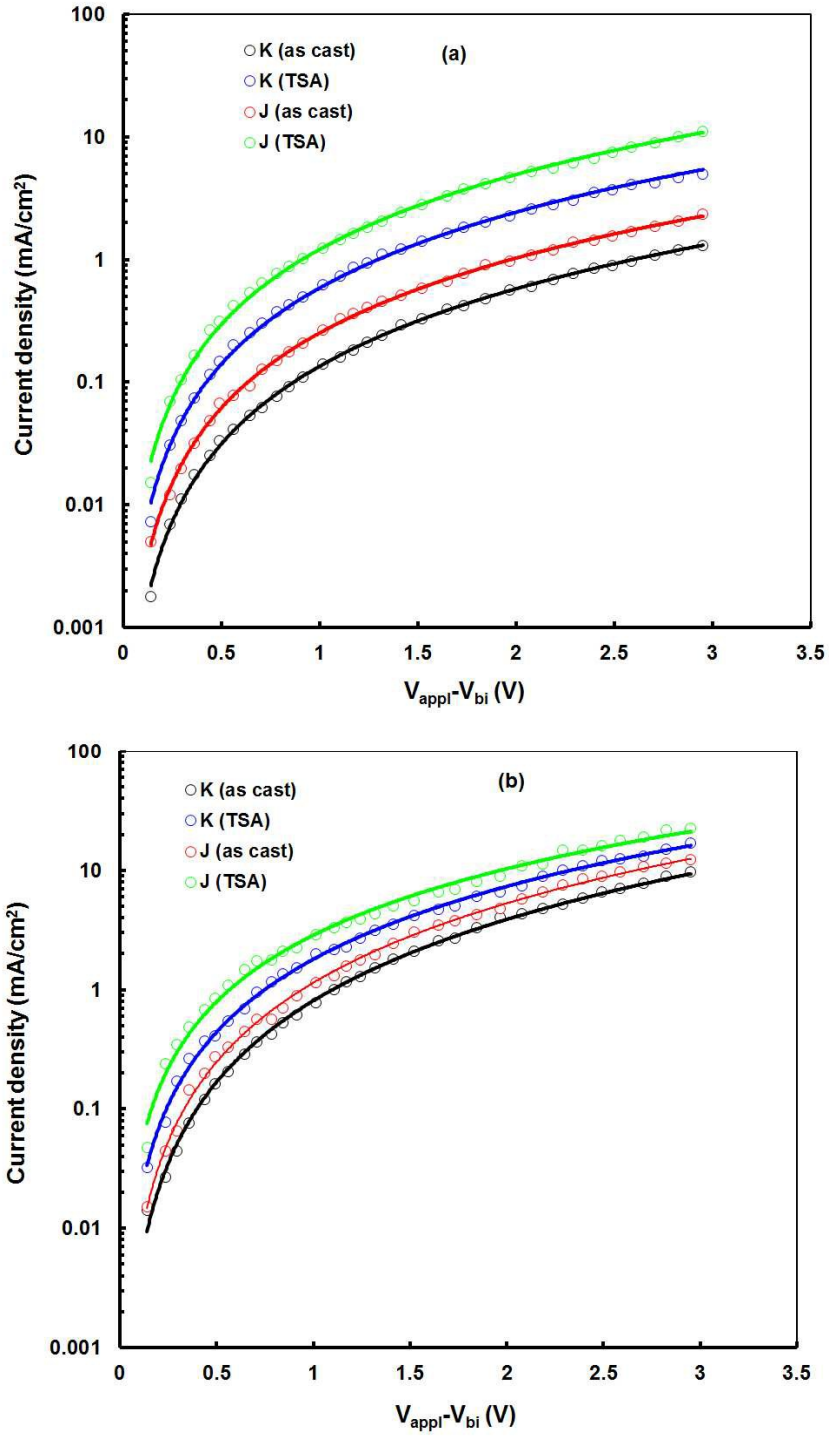

Figure 9 Dark J-V characteristics for (a) hole only and (b) electron only devices based on **J**:$PC_{71}BM$ and **K**:$PC_{71}BM$ active layers processed as cast and TSA treatment. The straight lines represent SCLC fitting.

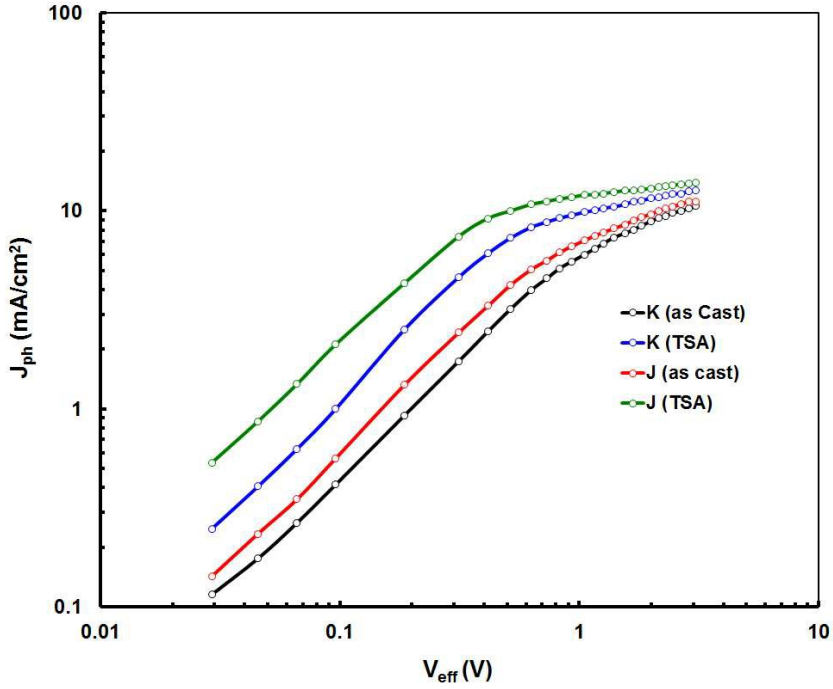

Figure 10 Variation of photocurrent density (J_{ph}) with the effective internal voltage (V_{eff}) for the devices based on based on **J**:$PC_{71}BM$ and **K**:$PC_{71}BM$ active layers processed as cast and TSA treatment.

TOC